JOURNAL OF GEOPHYSICAL RESEARCH: SPACE PHYSICS, VOL. 118, 6007–6018, doi:10.1002/2013JA018976, 2013

MHD numerical study of the latitudinal deflection of coronal mass ejection

Y. F. Zhou[1] and X. S. Feng[1]

Received 23 April 2013; revised 3 October 2013; accepted 6 October 2013; published 23 October 2013.

[1] In this paper, we analyze and quantitatively study the deflection of coronal mass ejection (CME) in the latitudinal direction during its propagation from the Corona to interplanetary (IP) space using a three-dimensional (3-D) numerical magnetohydrodynamics (MHD) simulation. To this end, 12 May 1997 CME event during the Carrington rotation 1922 is selected. First, we try to reproduce the physical properties for this halo CME event observed by the WIND spacecraft. Then, we study the deflection of CME, and quantify the effect of the background magnetic field and the initiation parameters (such as the initial magnetic polarity and the parameters of the CME model) on the latitudinal deflection of CMEs. The simulations show that the initial magnetic polarity substantially affects the evolution of CMEs. The "parallel" CMEs (with the CME's initial magnetic field parallel to that of the ambient field) originating from high latitude show a clear Equatorward deflection at the beginning and then propagate almost parallel to heliospheric current sheet and the "antiparallel" CMEs (with the CME's initial magnetic field opposite to that of the ambient field) deflect toward the pole. Our results demonstrate that the latitudinal deflection extent of the "parallel" CMEs is mainly controlled not only by the background magnetic field strength but also by the initial magnetic field strength of the CMEs. There is an anticorrelation between the latitudinal deflection extent and the CME average transit speed and the energy ratio $E_{\mathrm{cme}}/E_{\mathrm{sw}}$.

Citation: Zhou, Y. F., and X. S. Feng (2013), MHD numerical study of the latitudinal deflection of coronal mass ejection, *J. Geophys. Res. Space Physics*, *118*, 6007–6018, doi:10.1002/2013JA018976.

1. Introduction

[2] Coronal mass ejections (CMEs) are the most spectacular form of solar magnetic activity, during a typical CME 10^{11-13} kg of plasma are suddenly ejected toward the interplanetary (IP) space with velocities on the order of 100–1000 km s^{-1}, which can cause significant changes in coronal structure. It is well known that CMEs play an important role in space weather. They are responsible for nonrecurrent disturbances in the IP space, and their interactions with Earth's magnetosphere cause severe geoeffective storms.

[3] An understanding of the effects of CMEs on geospace is essential for forecasting the geospace weather. The Earth directed CMEs are the major cause for the severe geomagnetic storms, thus an important topic for space weather forecast is to predict whether or not a CME can be geoeffective. To understand the propagation trajectory of the CME, it is very important for us to predict whether or not a CME will hit the Earth and finally result in a geoeffective event. In fact, previous researchers have shown that CMEs may not propagate radially when they propagate from the corona to the IP space [e.g., *Cremades and Bothmer*, 2004; *Cremades et al.*, 2006; *Chané et al.*, 2005; *Jacobs et al.*, 2005; *van der Holst et al.*, 2005; *Wang et al.*, 2011; *Zuccarello et al.*, 2012]. *MacQueen et al.* [1986] found that 29 CMEs observed during the Skylab epoch undergo an average 2.2° equatorward deflection. They suggested that the equatorward deflections were due to the nonradial forces from the background large-scale bipolar magnetic field. *Wei and Dryer* [1991] found that all of the flare-associated shock waves tended to propagate toward the low-latitude region near the solar equator, and the fastest propagation directions tended toward the heliospheric current sheet (HCS) by statistically studying 149 flare-shock events based on interplanetary scintillation (IPS) observations. They suggested that this tendency is caused by the dynamic action of near-Sun forces and the HCS might have great influence on the propagation of solar transient disturbances in IP space. Also, the effect of the HCS on the shock propagation was studied by numerical simulations [e.g., *Odstrčil et al.*, 1996; *Smith et al.*, 1998]. *Jacobs et al.* [2005] and *van der Holst et al.* [2005] studied the influence of the background solar wind on the evolution properties of CMEs and the corresponding shocks by means of a 2.5-D (axisymmetric) ideal

[1]SIGMA Weather Group, State Key Laboratory of Space Weather, Center for Space Science and Applied Research, Chinese Academy of Science, Beijing, China.

Corresponding author: X. S. Feng, SIGMA Weather Group, State Key Laboratory for Space Weather, Center for Space Science and Applied Research, Chinese Academy of Sciences, Beijing 100190, China. (fengx@spaceweather.ac.cn)

2169-9380/13/10.1002/2013JA018976

magnetohydrodynamics (MHD) model. *Chané et al.* [2005, 2006] quantified the effect of the initial magnetic polarity of CMEs on the evolution properties and geoeffectiveness of CMEs by using a 2.5-D MHD simulation. They found that the CME from high latitude deflected toward the equator and hit the Earth when its initial CME magnetic field and the background wind magnetic field had the same polarity, while the same CME with an opposite polarity missed the Earth. In fact, the equatorward deflection propagation of the CME event during its outward propagation has been reported by *Cremades and Bothmer* [2004]. They statistically study 124 structured CME events observed by the Large Angle and Spectrometric Coronagraph (LASCO) during 1996–2002 and found that CMEs in activity-minimum years (1996–1998) systematically deflected 20° to lower latitudes. *Wang et al.* [2011] further confirmed the result by examining all the LASCO CMEs during 1997–1998. *Cremades et al.* [2006] found that the deflection of CMEs depended on the location and total area of coronal holes.

[4] CME deflections have become a very popular research topic since the NASA Solar Terrestrial Relations Observatory (STEREO) mission was successfully launched. For example, *Kilpua et al.* [2009] studied two high-latitude CMEs on 2 November 2008 using observations from STEREO and WIND spacecraft. They showed that the first CME was strongly deflected to the equator and suggested that the relative contribution of deflecting CMEs to the near ecliptic CME rate could be significant at solar minimum conditions. *Byrne et al.* [2010] quantified the deflection trajectory of 12 December 2008 CME event from high latitudes along the ecliptic by the 3-D reconstruction of CME front with the help of an elliptical tie-pointing technique. By introducing a theoretical method, *Shen et al.* [2011] analyzed the obvious deflection of the 8 October 2007 CME and found that the deflection of this CME might be caused by a nonuniform distribution of the background magnetic field energy density. *Bemporad et al.* [2012] and *Zuccarello et al.* [2012] found that the 21 September 2009 CME showed a deflection toward the HCS during its propagation due to an imbalance in the magnetic pressure and tension forces. Based on the SOHO and STEREO observations, the longitudinal deflections of CMEs were also suggested by some researchers [e.g., *Wang et al.*, 2004, 2006; *Liu et al.*, 2010a, 2010b; *Lugaz et al.*, 2010; *Gui et al.*, 2011].

[5] The main aim of this paper is focusing in particular on the deflection of CME in the latitudinal direction during its outward propagation. We will show the whole process of the CME propagation using a 3-D MHD simulation and quantitatively study the CME latitudinal deflection (LD) and the factors (the initial magnetic polarity, the parameters of CME model, and the background magnetic field) influencing it. In order to study the LD of the CME, we employ solar wind configurations at solar minimum, because the corona has a relatively simple configuration, and the current sheet is usually located near the Equator. To this end, we choose the background solar wind during Carrington rotation 1922, in which the well-studied halo CME event on 12 May 1997 was observed; the magnetic field on the Sun's surface used in our calculation is obtained from the Wilcox Solar Observatory at Stanford University (WSO).

[6] In the present paper, first, we will use a spherical plasmoid model to simulate the propagation of the 12 May 1997 CME eruption to 1 AU. Then we analyze the propagation trajectory of CME during its outward propagation. The paper is organized as follows. A brief description of simulation model is presented in section 2. Section 3 gives the simulation of the halo CME event that occurred on 12 May 1997. The analysis of the propagation trajectory of CMEs is given in section 4. Finally, we summarize the results in section 5.

2. Description of the Simulation Model

[7] In the present paper, the solar wind model is performed using the 3-D SIP-CESE MHD model described by *Zhou et al.* [2012]. This model can reproduce the solar wind background by means of an artificial heating/acceleration source term in the energy equation, which is given by

$$S_E = Q_0 \cdot \frac{1}{f_s} \exp(-r/L_Q), \tag{1}$$

where the constant value $Q_0 = 1.0 \times 10^{-6}$ J m^{-3} s^{-1}, and the decay length of heating L_Q is set to be $0.9R_s$. The expansion factor $f_s = \left(\frac{R_s}{r}\right)^2 \frac{B_{R_s}}{B_r}$ where B_{R_s} is a magnetic field at the solar surface, and r is the distance from the solar center. For the specific heat ratio γ, similar to that of *Jacobs and Poedts* [2011], a variable polytropic index is used:

$$\gamma = \begin{cases} \gamma_0 & \text{if} \quad r < r_1, \\ \gamma_0 + (\gamma_1 - \gamma_0)\sin^2\left(\frac{\pi}{2}\frac{r-r_1}{r_2-r_1}\right) & \text{if } r_1 \le r \le r_2, \\ \gamma_1 & \text{if} \quad r > r_2, \end{cases} \tag{2}$$

where the value of γ is smoothly varying between the value γ_0 close to the Sun, where $\gamma_0 = 1.2$ and its value, $\gamma_1 = 1.46$, near 1 AU. The variation in γ takes place between the radial distances r_1 and r_2, where r_1 and r_2 are taken to be $1R_s$ and $20R_s$, respectively. The temperature and plasma density at the inner boundary are typically taken to be 1.5×10^6 K and 1.67×10^{-13} kg m^{-3}, respectively. The computational domain covers $-90° \le \theta \le 90°, 0° \le \phi \le 360°$, and $1R_s \le r \le 235R_s$.

[8] Here we simulate the steady state solar wind with the observed photospheric magnetic field and Parker's 1-D solar wind solution [*Parker*, 1963] as the initial values. The details of computing the steady state solar wind were given in *Feng et al.* [2007, 2010] and thus are omitted here. Figure 1a depicts a 2-D cut of magnetic structure and velocity for the steady state solar wind in the solar corona (SC) domain in the meridional plane. Figure 1b shows the three-dimensional heliospheric current sheet in the inner heliospheric (IH) domain. The color contours indicate the radial speed, while the magnetic field is represented by solid black lines. From the figures, we can see that the coronal field structure has a typical characteristic at solar minimum when the corona has a relatively simple configuration. The coronal magnetic field is dominated by a dipole pattern, and the HCS is nearly in the heliospheric equatorial plane, and the latitudinal excursion of HCS is very limited. A helmet streamer is formed at low latitude around the equator with low radial speed. An open configuration of the magnetic field is achieved at high latitudes with high radial speed. We can see that the steady state solar wind reveals an approximate bimodal outflow pattern, slow-speed wind leaves the Sun around 350 km s^{-1} near

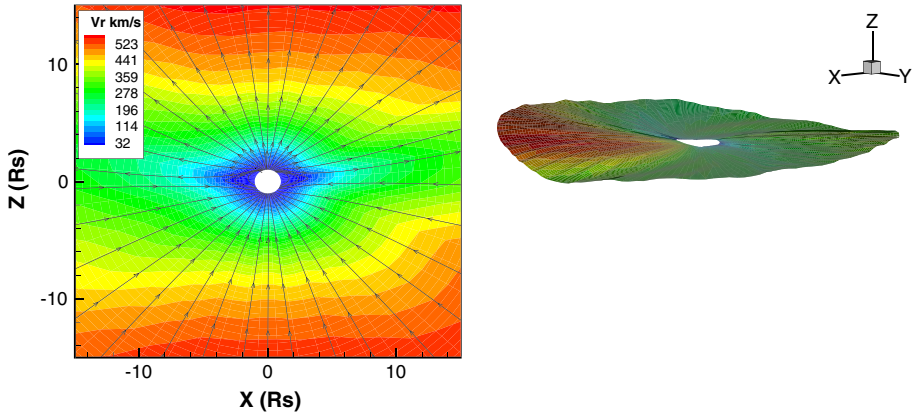

(a) (b)

Figure 1. (a) Magnetic field and radial speed for the steady state solar wind solution in the SC domain in the solar-terrestrial meridian plane. (b) Steady state current sheet in the IH domain. The color contours represent the radial speed.

the current sheet region, and high-speed wind leaves above 600 km s^{-1} in the high-latitude region.

[9] To initiate a CME, some researchers have proposed a lot of theoretical models, for example, the photospheric converging and shear motions [*Forbes et al.*, 1994; *Mikic and Linker*, 1994; *Antiochos et al.*, 1994], flux emergence [*Feynman and Martin*, 1995; *Chen and Shibata*, 2000], and flux cancelation [*Zhang et al.*, 2001]. However, so far, there is no general consensus yet on the triggering mechanism. In this paper, we superpose a very simple spherical plasmoid model on the background solar wind to initiate the CME. This simple model gives us an easy way to investigate the propagation of the CME from the corona to IP space, although it does not have complicated features. We briefly describe the CME initiation model, while more detail is discussed in our previous paper [*Zhou et al.*, 2012], in which we have successfully simulated some important features of 4 Nov 1997 CME event observed by WIND spacecraft.

[10] The density, temperature and radial velocity profile of the initial perturbation are defined as follows:

$$\begin{aligned} \rho &= \rho_0 + \rho_{\max}\left(1 - a^2/a_{\rm cme}^2\right) \\ T &= T_0 + T_{\max}\left(1 - a^2/a_{\rm cme}^2\right) \\ v_r &= v_{r0} + v_{\max}\left(1 - a^2/a_{\rm cme}^2\right) \end{aligned} \tag{3}$$

where $a_{\rm cme}$ is the radius of the plasmoid, a denotes the distance from the center of the plasmoid, and ρ_0, v_{r0}, and T_0 are the density, radial velocity, and temperature of the background solar wind, respectively. $\rho_{\max}$, $v_{\max}$, and $T_{\max}$ are the maximum density, radial velocity, and temperature added on the ambient solar wind, respectively.

[11] The initial magnetic field of the spherical plasmoid is assumed to take the form as that in *Zhou et al.* [2012] in local spherical coordinates $(r^\ell, \theta^\ell, \phi^\ell)$:

$$\begin{aligned} B_{r^\ell} &= (2B_0/\alpha r^\ell)\, j_1(\alpha r^\ell)\cos\theta^\ell \\ B_{\theta^\ell} &= -(B_0/\alpha r^\ell)[\sin(\alpha r^\ell) - j_1(\alpha r^\ell)]\sin\theta^\ell \\ B_{\phi^\ell} &= \pm B_0\, j_1(\alpha r^\ell)\sin\theta^\ell \end{aligned} \tag{4}$$

where B_0 is a constant, and $\alpha = 4.493409458 a_{\rm cme}^{-1}$ is the constant derived from the force-free condition of $\nabla \times \mathbf{B} = \alpha \mathbf{B}$ with the boundary condition of $B_{r^\ell} = 0$ at $r^\ell = a_{\rm cme}$. $j_1(x)$ is the spherical Bessel function, $j_1(x) = x^{-2}\sin x - x^{-1}\cos x$. If the parameter α is negative, then the initial magnetic field assumes a left-handed configuration. The spherical plasmoid superposed on the solar wind is initially not in equilibrium with its external environment, so it will rapidly expand as it is expelled from the corona.

3. Comparison Between Simulated and In Situ Data

[12] The 12 May 1997 famous halo CME event began at approximately 04:35 UT, when an eruptive event was observed by EIT in the lower corona. The eruptive event observed in EIT was centered on active region AR8038 at N21W07 [*Thompson et al.*, 1998]. The halo CME was first seen by SOHO/LASCO's C2 coronagraph at 05:30 UT, and it was first visible in C3 image in a frame recorded at 08:06 UT, respectively. The shock produced by the interplanetary coronal mass ejection (ICME) arrived at WIND spacecraft at about 01:00 UT on 15 May 1997 followed by a magnetic cloud. The transit time of the disturbance from the Sun to Earth was approximately 75 h. This is close to the average transit time of 80 h derived from a statistical study of all Earth-directed events observed during 1996–1997 [*Brueckner et al.*, 1998]. The corresponding average speed of the disturbance over a distance of 1 AU is about 550 km s^{-1}. More details on the solar observations are given in *Thompson et al.* [1998] and *Plunkett et al.* [1998].

[13] Here we empirically choose the parameters in the CME model to try to match the WIND data. The CME's center is placed at $2.0R_s$, and the radius of the initial CME, $a_{\rm cme}$, is $0.8R_s$. The value of $v_{\max}$ is set to be 600 km s^{-1}. $\rho_{\max}$ and $T_{\max}$ are set to be five times and three times the ambient solar wind value at the center of the CME, respectively. The maximal magnetic field strength B_0 is 5.0 G. The CME is initially centered at N21W07 to conform to the location of the observed flare/CME. For a better agreement with the IMF observed by spacecraft, the polar axis

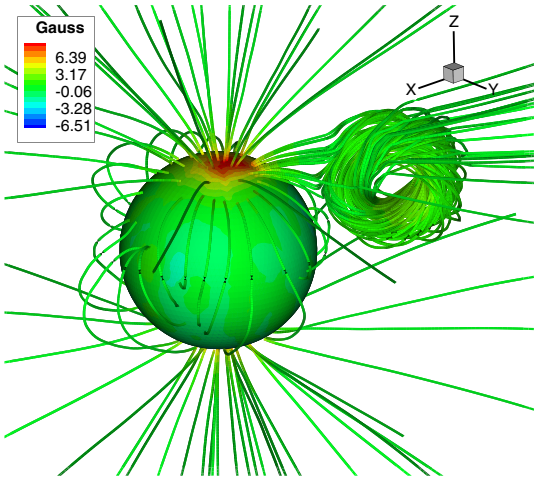

Figure 2. Three-dimensional view of the initial coronal magnetic field. Field lines of the CME are shown in color to illustrate the magnetic field strength. The color contours represent the radial magnetic field strength on the solar surface.

of the ejected spheromak is rotated toward the negative y axis direction to make it incline about 5° from the negative y axis. The initial plasma plasmoid has added to the corona 8.22×10^{24} J of magnetic energy, 3.89×10^{23} J of kinetic, and 1.76×10^{24} J of thermal energy. The increase in total energy (magnetic + kinetic + thermal energy) is 1.04×10^{25} J. Here we estimate the energy injected into the computation domain by $\triangle E = E_1 - E_0$, where E_1 (E_0) is the energy after (before) CME initiation. The magnetic, kinetic, and thermal energy values are calculated using the expressions: $E_m = \int_A \frac{B^2}{2} \mathrm{d}A$, $E_k = \int_A \frac{1}{2}\rho V^2 \mathrm{d}A$, $E_t = \int_A \frac{p}{\gamma - 1} \mathrm{d}A$, respectively. In the simulation, we take 04:35 UT on 12 May 1997, when EIT first observed the CME in the lower corona, to be the initial time of the eruption. The 3-D schematic picture of the initial coronal magnetic field at $t = 0$ is shown in Figure 2.

[14] Figure 3 displays the comparison of our numerical results at 1 AU and the WIND spacecraft data. As seen from this figure, although using a simple CME model, our simulation successfully reproduces many basic structures of the in situ measurement, such as the similar curves of the plasma density, an increase in the magnetic field magnitude, in particular the behaviors of magnetic field component: B_y and southward B_z, and the large-scale smooth magnetic field rotation. In order to better compare our results and the WIND observation, we shift 6 h ahead to the time axis of simulated profiles. This is probably related to the wind density: the magnetic cloud is slowed down by the high density of the background wind. The computed magnetic field is multiplied by 2, because it is nearly half of that observed. This may be due to the small background magnetic field, which is caused by the imperfectness of potential field source surface model and the coarse grid resolution in IP space. And there are some differences between the simulated x component of the magnetic field and the observed data. Despite its shortcomings, our simulation gives the main features of the CME to fit the in situ data at 1 AU.

[15] From the figure, we can see that the shape of the density curve at 1 AU is well reproduced in this simulation, but the simulated values are higher than that observed. This is because the density of the simulated background solar wind is higher than that observed. Meanwhile, from this figure, the simulated background velocity is greater than that observed. The reason for this may be due to the single fluid model used, the volumetric heating assumption and other reasons as pointed out by *Feng et al.* [2010]. For the y and z components of the magnetic field, we find that the simulated and measured profiles at 1 AU are very similar. From the computed B_z at 1 AU shown in Figure 3, we find that the field turns southward at $\sim$ 10:00 UT on 15 May 1997 for 19 h, reaching a minimum –10 nT. Then the magnetic field smoothly rotates northward reaching a maximum 3.5 nT, lasting more than 20 h. The south-north rotation of this magnetic field component is mainly due to the passage through the helical field of the CME mentioned by *Wu et al.* [1999]. The strong south-north rotation of the IMF and prolonged southward IMF shown is responsible for a strong magnetospheric response.

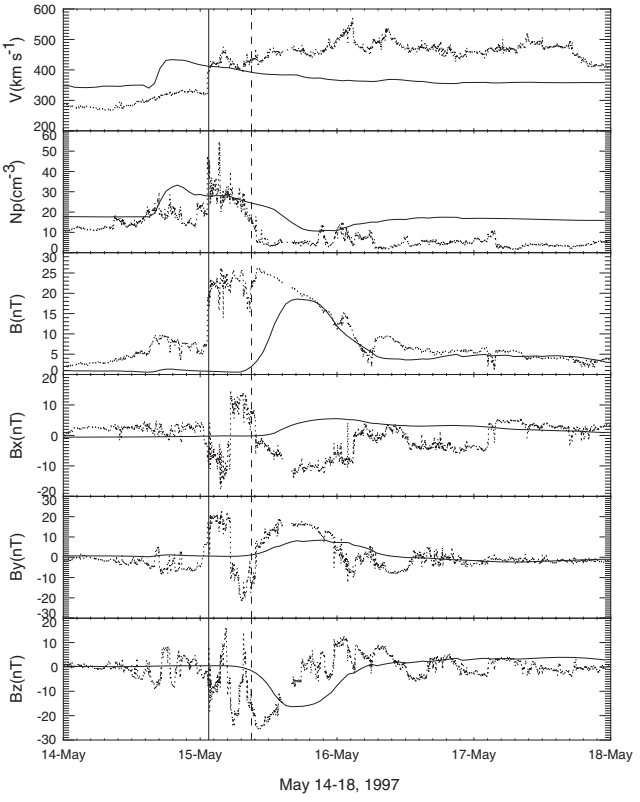

Figure 3. Comparison between the in situ data obtained by the WIND spacecraft and our simulation during the 12 May 1997 event. (top to bottom) Flow velocity, number density, magnetic field, and three components of magnetic field in geocentric solar ecliptic (GSE) coordinates. The vertical solid line indicates the time of the ICME-driven shock. The vertical dashed line indicates the starting time of the magnetic cloud. The simulated results at the Earth are shown by the solid lines. The WIND observations are shown by the dotted lines.

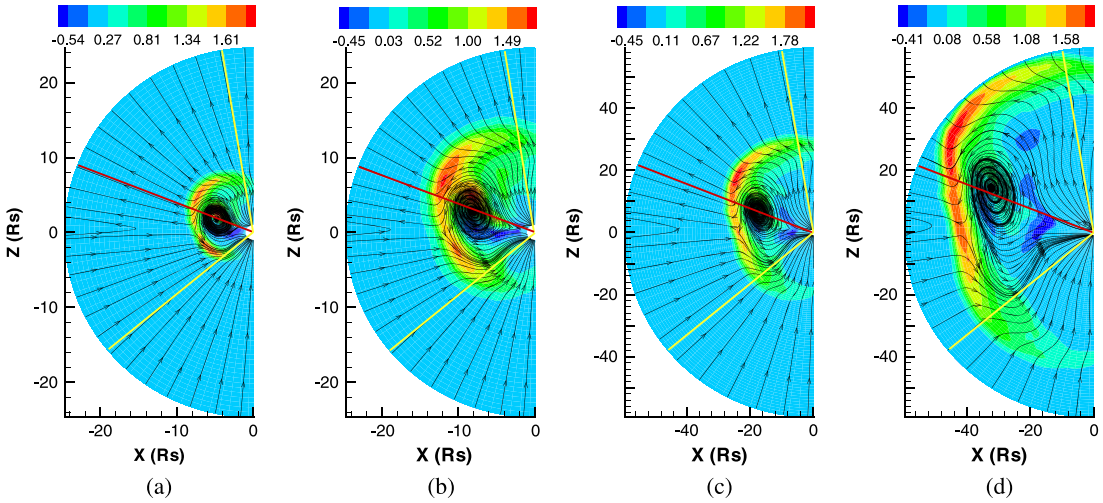

Figure 4. Contour plots of the relative density distribution for the CME on the solar-terrestrial meridian plane after 1.0, 2.0, 5.0 and 10.0 h. The black lines represent the magnetic field. The relative density is defined as follows: $\overline{\rho} = (\rho - \rho_{wind})/\rho_{wind}$.

4. Analysis of the Propagation Trajectory of CMEs

[16] In what follows, we will study the propagation trajectory of CMEs and analyze the factors that influence the propagation trajectory of the corresponding CME, in particular the LD of CME during its outward propagation up to IP space. Figure 4 shows the evolution of CME on the solar-terrestrial meridian plane at four different instants (t = 1.0, 2.0, 5.0and 10.0 h) after adding the force-free configuration, traveling from the corona to IP space. The red lines in the panels show the position angle of 12 May 1997 CME event observed, which is at the northern hemisphere 21°. The yellows lines are 60° north and south away from the observed position angle of CME. From the figure, we find that this CME shows an equatorward deflection.

[17] Why does the CME deflect toward the low-latitude region near the solar equator (roughly symmetrical to the heliospheric current sheet)? We can explain the reason by applying the theoretical method proposed by *Shen et al.* [2011] to the CME, in which the direction and magnitude of the deflection are well consistent with the gradient (with the conventional minus sign in front) of magnetic energy density, $< -\nabla\omega >$, where $\omega = \frac{B^2}{2\mu_0}$ is the magnetic energy density. The magnetic energy density distribution of the simulated steady state solar wind at $3R_s$ is shown in Figure 5a. The asterisk sign in the figure denotes the associated source location of the halo CME. From this figure, we find that the distribution of the background magnetic energy density is nonuniform. The black dashed line in the figure shows the corresponding position of the HCS, which separates regions of the solar wind where the magnetic field points toward or away from the Sun. We can see that the magnetic energy density increases gradually above and below the HCS, and the direction of the magnetic energy density

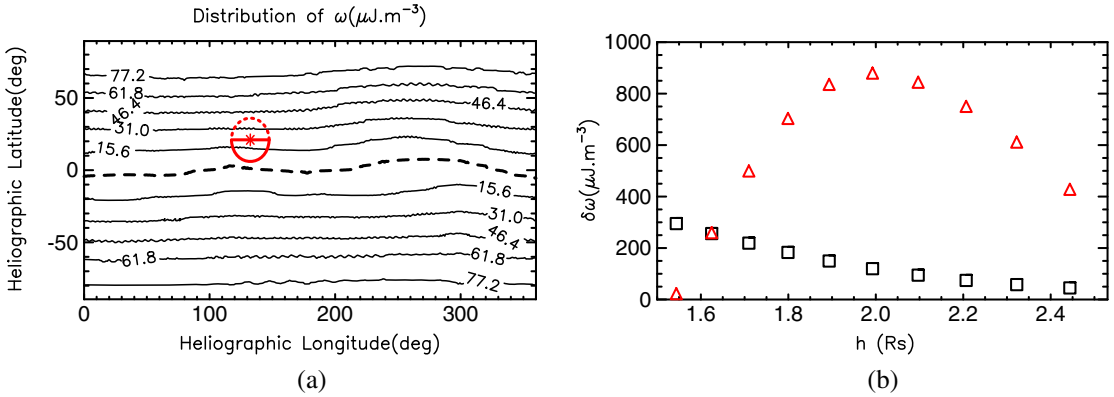

Figure 5. (a) Distribution of the magnetic energy density ω at the height of $3R_s$. The dashed line shows the neutral line at this height. The red asterisk sign shows the position of this CME at the height. The regions enclosed by the red dotted line and the solid line show the selected upper and lower parts, respectively. (b) The variation of $\delta\omega$ of the CME (red triangles) and the background magnetic energy density (black squares) with the height.

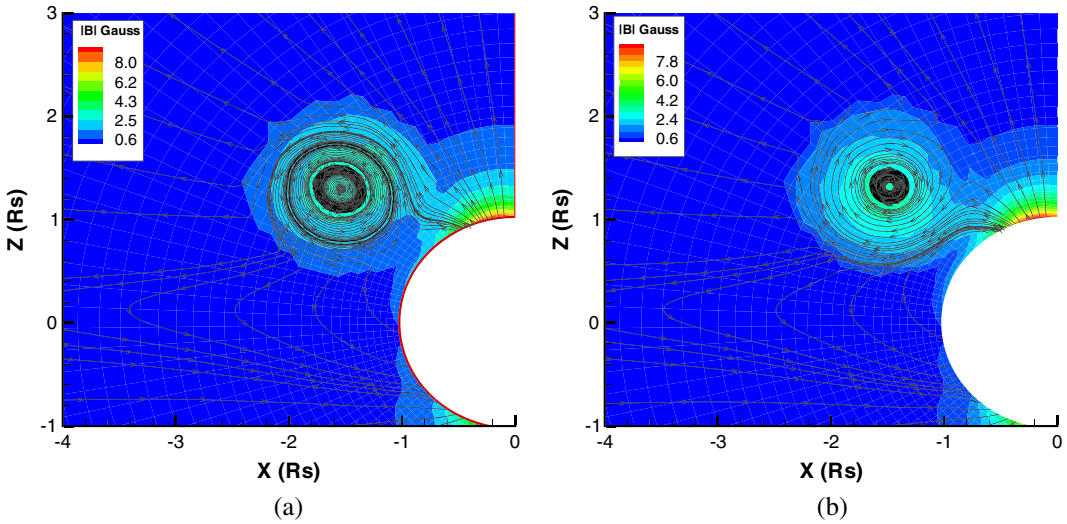

Figure 6. Schematic picture of the initial magnetic field configuration in the $y = 0$ plane in (a) Case A ("parallel" CME) and (b) Case B ("anti-parallel" CME). The color contours represent the magnetic field strength.

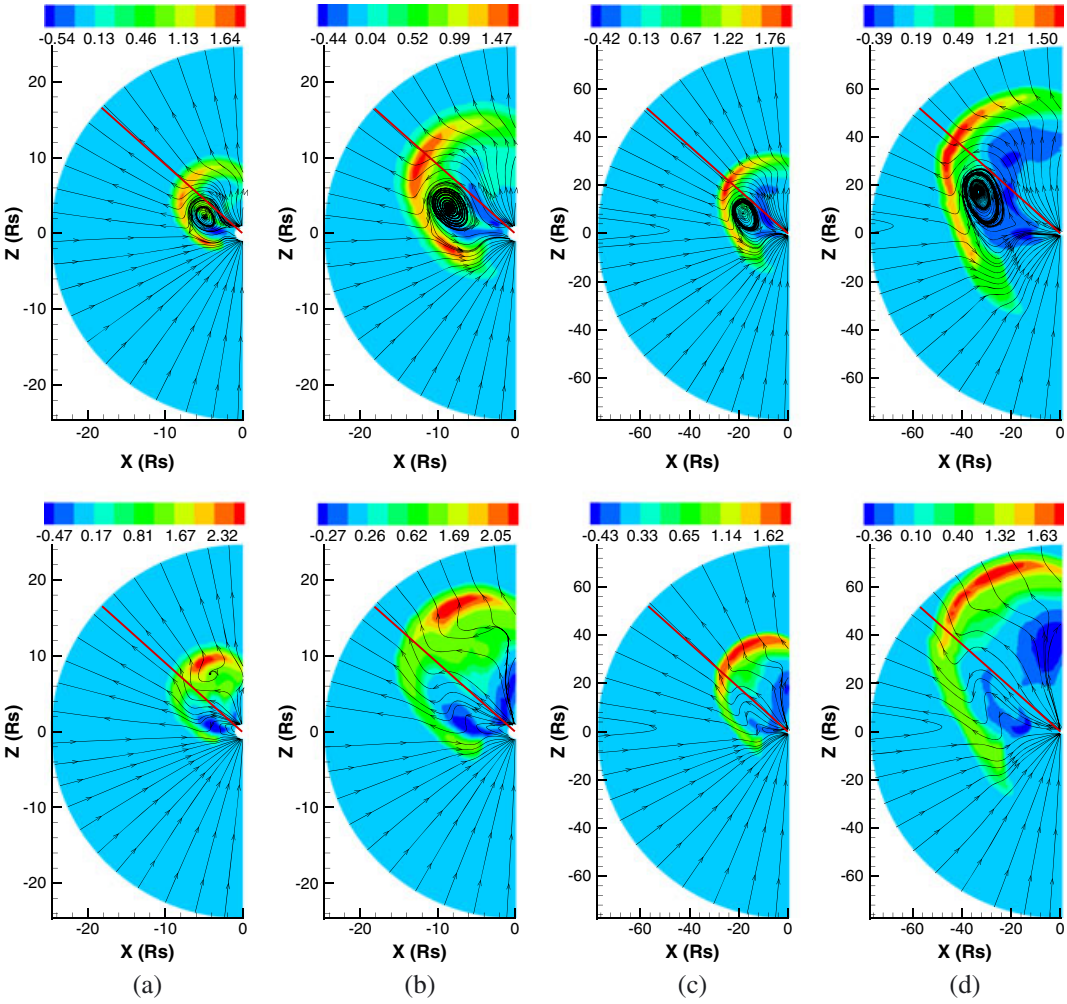

Figure 7. Contour plots of the relative density distribution for the CME on the solar-terrestrial meridian plane after (a) 1.0, (b) 2.0, (c) 5.0, and (d) 10.0 h. The black lines represent the magnetic field. (top row) "parallel" CME; (bottom row) "anti-parallel" CME.

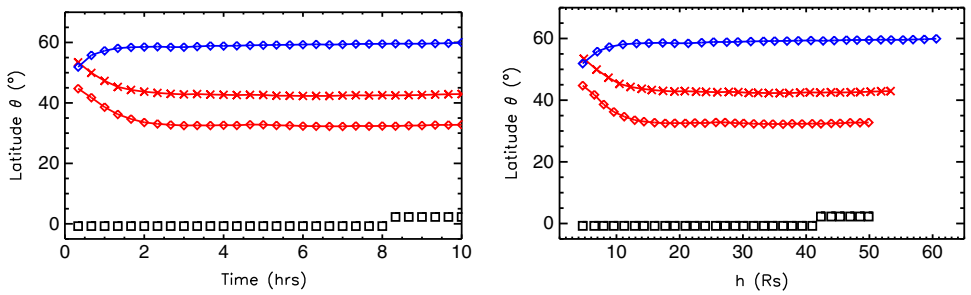

Figure 8. The propagation trajectory of Case A (red diamonds), Case B (blue diamonds), and Case C (red crosses). The squares indicate position angles of HCS. (a) The latitude-time and (b) latitude-height plots.

gradient is toward the HCS, where the magnetic energy density is lowest. The magnetic energy density gradient makes the CME deflect to the region with lower magnetic-energy density. The figure mainly reflects the influence of this background magnetic energy density on CME deflection in the latitudinal direction. This magnetic configuration, due to the nonradial magnetic energy density gradient, will supply a force compelling the ejecta to move toward the low-latitude region.

[18] We also analyze the variation of $\delta\omega$ in the corona near the associated source location of the halo CME in Figure 5b, where $\delta\omega = \omega_U - \omega_L$ and ω_U and ω_L are the average energy density in the upper and the lower part of the simulated CME, respectively. The CME-perturbed magnetic field will act an Equatorward force on the CME if $\delta\omega$ is positive, while a polarward force would act on the CME when $\delta\omega$ is negative. The regions enclosed by the red dotted line and the red solid line in Figure 5a show the selected upper part and lower part in a 15° angle range. The squares in Figure 5b show the variation of $\delta\omega$ of the simulated background magnetic energy density, and the red triangles show the variation of $\delta\omega$ after CME initiation. From the figure, we find that $\delta\omega$ of the CME and the background magnetic energy density are positive. $\delta\omega$ of the CME reaches maximum at $2R_s$, then it gradually decreases along the distance. The result means that an equatorward force is acting on the CME and could deflect the CME to a lower latitude.

[19] In the following, we study the factors influencing the deflection propagation of the CME. We first analyze and quantify the effect of the initial flux rope magnetic field polarity on the evolutionary features of the CMEs in IP space. Depending on the parameter α, we carry out two different cases of CMEs simulations. In the above simulation, $\alpha > 0$, the magnetic field direction of the CME on the solar-terrestrial meridian plane is parallel to that of the background solar wind, which is referred as "parallel" CME. When $\alpha < 0$, the magnetic field direction of the CME on the solar-terrestrial meridian plane is antiparallel to that of the background magnetic field, which is referred as "antiparallel" CME. In order to better study the characteristics of the CME propagation, in particular the LD of CME, the "parallel" CME and "antiparallel" CME are launched at higher latitude and the same longitude of the halo CME simulated above: such as N41W07. The two CMEs are labeled as Cases A and B, respectively. Figure 6 shows schematic pictures of the initial magnetic field on the meridional plane through the center for Case A (Figure 6a) and Case B (Figure 6b). In the numerical simulations, the CMEs have the same initial density, temperature, velocity, and magnetic field strength.

[20] Figure 7 shows the evolution of the CMEs on the solar-terrestrial meridian plane at four different instants (t = 1.0, 2.0, 5.0 and 10.0 h) for Cases A and B, respectively, traveling from the corona to IP space. The top row shows the result of Case A, the bottom row displays the result of Case B. The red lines in the figures show the position angle of CMEs which are launched at N41. From the figure, it is clear that the "parallel" CME shows an equatorward deflection. Because the HCS is located near the solar equator during this period, the "parallel" CME deflects to the HCS. The "anti-parallel" CME veers toward the pole, because the direction of the background magnetic field is opposite to the magnetic field of the CME, and a strong magnetic reconnection occurs. From the bottom row of Figure 7, we find that the magnetic flux of the flux rope is peeling off due to the reconnection with the background field as CME propagates outward. Finally, the flux rope no longer exists after most of the magnetic flux is reconnected.

[21] In order to quantitatively study the evolution path and LD of CME, we define the 2-D center and CME central

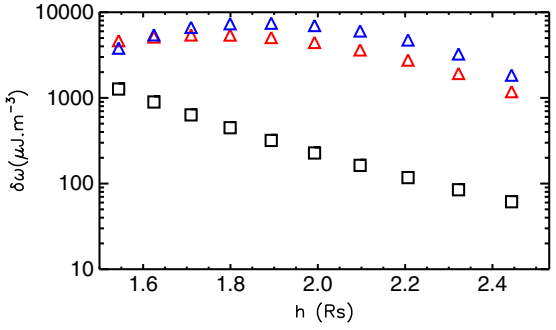

Figure 9. The variation of $\delta\omega$ of the background magnetic energy density (squares). The variation of $\delta\omega$ for Case A (red triangle). The variation of $\delta\omega$ with the minus sign for Case B (blue triangles).

Table 1. Physical Characteristics of the Perturbations and Their Corresponding Energy Contents for All 11 Cases of the Numerical Experiments

Case	δ_B	δ_ρ	δ_T	δ_V	Magnetic Energy (J)	Kinetic Energy (J)	Thermal Energy (J)	Total Energy (J)
1	5.0	5	3	600	8.13×10^{24}	2.78×10^{23}	1.06×10^{24}	9.47×10^{24}
2	5.0	10	3	600	8.13×10^{24}	4.77×10^{23}	1.85×10^{24}	1.05×10^{25}
3	5.0	5	6	600	8.13×10^{24}	2.78×10^{23}	1.79×10^{24}	1.01×10^{25}
4	5.0	5	3	300	8.13×10^{24}	8.72×10^{22}	1.06×10^{24}	9.28×10^{24}
5	3.0	5	3	600	2.94×10^{24}	2.78×10^{23}	1.06×10^{24}	4.28×10^{24}
6	3.0	10	3	600	2.94×10^{24}	4.77×10^{23}	1.85×10^{24}	5.27×10^{24}
7	3.0	5	6	600	2.94×10^{24}	2.78×10^{23}	1.79×10^{24}	5.01×10^{24}
8	3.0	5	3	300	2.94×10^{24}	8.72×10^{22}	1.06×10^{24}	4.09×10^{24}
9	5.0	10	3	600	8.13×10^{24}	3.11×10^{23}	1.15×10^{24}	9.58×10^{24}
10	5.0	10	3	600	8.13×10^{24}	4.05×10^{23}	1.81×10^{24}	1.03×10^{25}
11	5.0	10	3	600	8.13×10^{24}	2.50×10^{23}	8.93×10^{23}	9.21×10^{24}

latitude on the solar-terrestrial meridian plane by the relative mass:

$$\mathrm{CORM}(r) = \frac{\sum_{ij} \bar{\rho}_{ij} r_i^2 \mathrm{d}r_i \mathrm{d}\theta_j}{\sum_{ij} \bar{\rho}_{ij} r_i \mathrm{d}r_i \mathrm{d}\theta_j}, \quad \mathrm{CORM}(\theta) = \frac{\sum_{ij} \bar{\rho}_{ij} \theta_j r_i \mathrm{d}r_i \mathrm{d}\theta_j}{\sum_{ij} \bar{\rho}_{ij} r_i \mathrm{d}r_i \mathrm{d}\theta_j}$$

where $\bar{\rho}$ denotes the relative density (identified by the 20% enhancement of the density, that is, $\bar{\rho} = 1.2\rho_{\mathrm{wind}}$), and the indices i and j run over all grid points in the radial and azimuthal directions on the solar-terrestrial meridian plane, respectively.

[22] Figure 8 shows the propagation trajectory of CME central latitude on the solar-terrestrial meridian plane after 10 h for Cases A and B, respectively. Figure 8a shows the latitude-time profiles, and Figure 8b shows the latitude-distance profiles. Here we record once every 20 min. The squares in the figure show the position angles of HCS at different heights. The red diamonds show the propagation trajectory of the CME central latitude for Case A, and the blue diamonds show the result of Case B. We can see that the "parallel" CME deflects to the HCS and the "antiparallel" CME deflects toward the polar region at the beginning, then the CMEs propagate almost along the radial direction in IP space. This is similar to the scenario of *Chané et al.* [2005]. From the figure, we find that the "parallel" CME shows a deflection of about 8.5° toward the HCS during its outward propagation from the corona to IP space, and the "anti-parallel" CME shows a deflection of about 18° toward the pole.

[23] The reason of these different configurations between Cases A and B is shown in Figure 9, which shows the variation of $\delta\omega$ in the corona near the center of the CMEs. The squares in the figure show the variation of $\delta\omega$ of the background magnetic energy density, the red triangles in the figure show the variation of $\delta\omega$ after CME initiation for Case A, and the blue triangles show the result of Case B with the minus sign in front. From the figure, we find that $\delta\omega$ of the background magnetic energy density at N41W07 is larger than that of the background magnetic energy density at N21W07 (compare with Figure 5). $\delta\omega$ of coronal magnetic energy density after CME initiation is positive for the "parallel" CME but is negative for the "anti-parallel" CME. This indicates that an equatorward force is acting on the "parallel" CME, and it could be deflected to a lower latitude. A polarward force is acting on the "anti-parallel" CME, and it could be deflected to a higher latitude.

[24] We simultaneously simulate the CME from higher latitude, which is launched at N61W07 and has the same polarity as that of Case A; the CME is labeled as Case C. We show the propagation trajectory of CME central latitude on the solar-terrestrial meridian plane after 10 h for Case C in Figure 8 using the red crosses. From the figure, we find that Case C shows a deflection of about 18° toward the HCS. The deflection extent is larger than that of Case A, because the magnetic density gradient at higher latitudes is stronger.

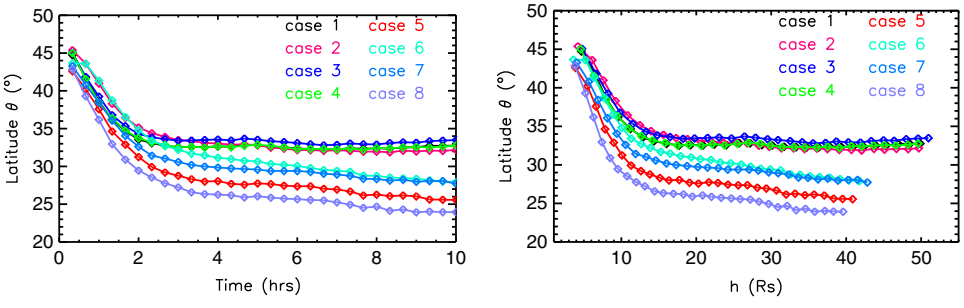

Figure 10. The propagation trajectory for the eight cases. (a) The latitude-time plot and (b) latitude-height plot.

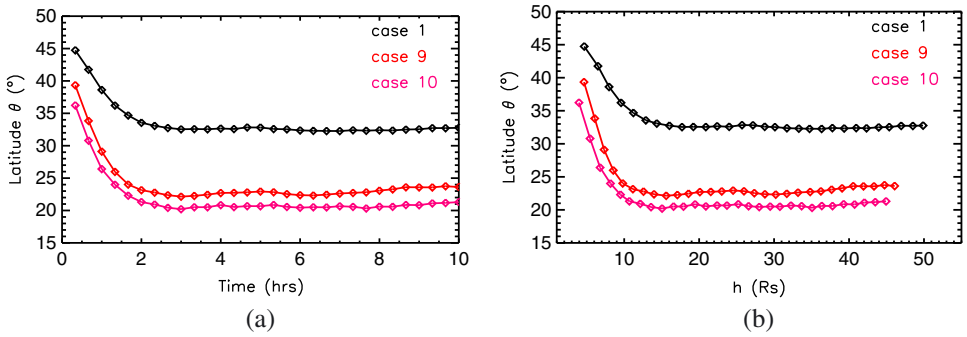

Figure 11. The propagation trajectory for Case 1, Case 9, and Case 10. (a) The latitude-time plot and (b) latitude-height plot.

This result indicates that during solar minimum, even CMEs that are originated from high latitude can be easily deflected toward the Equator and eventually result in geoeffective events. From the results of Figure 8 above, we find that the CME deflection almost occurs within the corona. In the corona, the magnetic field is dominant, the magnetic energy density gradient makes the CME deflect to the low magnetic-energy density region. The magnetic energy density gradient decreases quickly when a CME propagates outward. When the CME propagates into the interplanetary space, a weak magnetic energy density gradient is not sufficient to make the CME deflect.

[25] In fact, we are most interested in the CME that deflects toward the Equator. In the following, we will study the effect of the four parameters of the CME model on the equatorward deflection of CME. So we perform a total of eight cases of numerical experiments by adjusting the four parameters of the CME model: decreasing the magnetic field, increasing the density and temperature, and decreasing the velocity, based on Case A (referred as Case 1 hereafter). Wherein Cases 2–5 are performed by adjusting the four parameters based on Case 1, and Cases 6–8 are performed by adjusting the other three parameters except the magnetic field parameter based on Case 5. To obtain these results, the amplitudes of the four perturbations (B, ρ, T, and V) are scaled by δB, $\delta\rho$, δT, and δV, respectively. Quantitatively, the values $\delta B = 5$ and $\delta B = 3$ mean that the maximal magnetic field strength B_0 is 5.0 G and 3.0 G, respectively. Similarly, $\delta V = 300$ (600) means that the value of v_{max} is set to be 300 (600) km s^{-1}. $\delta\rho = 5$ (10) corresponds to a density rise of a factor of 5 (10) from the background solar wind at the center of the CME; and $\delta T = 3$ (6) corresponds to a temperature rise of a factor of 3 (6). The experiments are carried out by using these various perturbations with the corresponding energy inputs shown in Table 1. Figure 10 shows the propagation trajectory of CME central latitude on the meridian plane after 10 h for the eight cases in Table 1.

[26] From the figure, we find that Case 5 shows a deflection of about 15.5° toward the HCS; the deflection extent of Case 5 is clearly larger than that of Case 1. But the deflection extent of Cases 2–4 is almost the same as that of Case 1, and the difference between the deflection extent of Cases 6–8 and that of Case 5 is also very small. So it results that the magnetic field parameter of CME model has the greatest impact on the propagation trajectory of the CME, and that the smaller the magnetic field strength is, the larger the deflection extent is. The reason is that the magnetic field freezing-in effect can restrain the ejecta to move toward the low-latitude region, and the magnetic field freezing-in effect is weaker when magnetic field parameter is smaller. However, the other three parameters do not have significant effect on the propagation trajectory of the CME.

[27] We also study the effect of the background magnetic field on the propagation trajectory of the equatorward

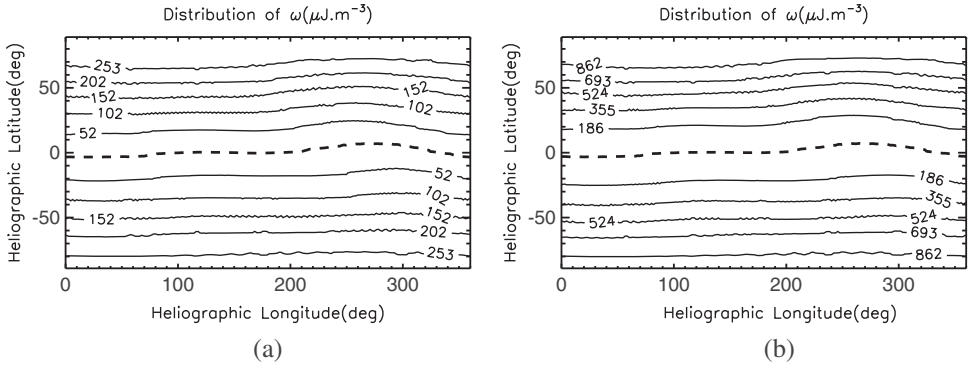

Figure 12. Distribution of the magnetic-energy density ω at the height of $3R_s$ for Case 9 and 10, respectively. The dashed lines show the neutral lines at this height.

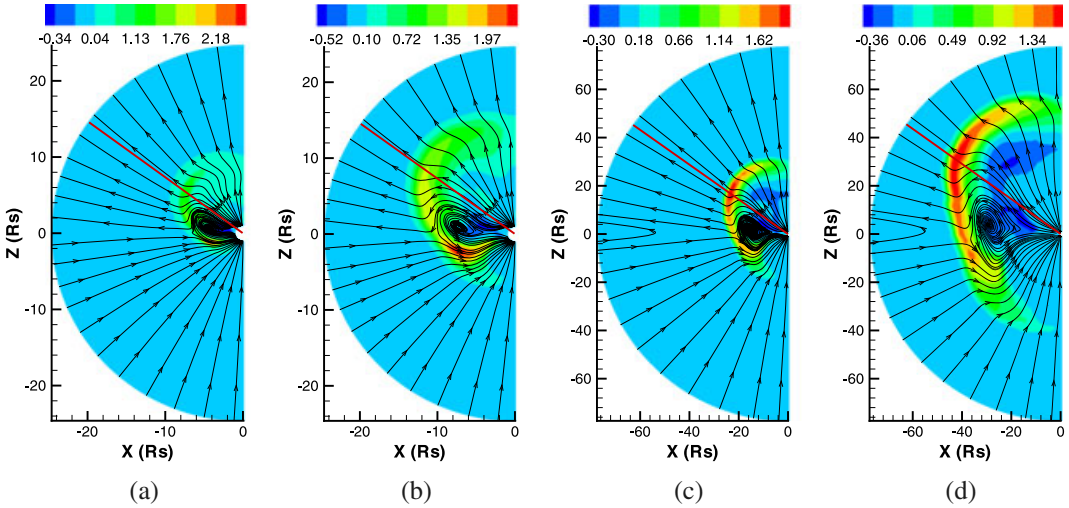

Figure 13. The evolution of the CMEs on the solar-terrestrial meridian plane at four different instants (t = (a) 1.0, (b) 2.0, (c) 5.0, and (d) 10.0 h) for Case 9. The black lines represent the magnetic field.

deflection of CME. For example, we compute the background solar wind with two times (Case 9) and four times (Case 10) the observed photospheric magnetic field. Based on the two types of background wind, we study the propagation trajectory of the CME, which has the same initial conditions as that of Case A, including the polarity. Figure 11 shows the propagation trajectory of the CME central latitude of the Cases 9–10 on the solar-terrestrial meridian plane. From the figure, we find that Case 9 shows a deflection of about 17° toward the HCS, and the deflection extent of Case 10 is about 18°. By comparing the result of Case 1, we find that the background magnetic field substantially affects the propagation trajectory of the CMEs. It is clear that the larger the background magnetic field strength is, the larger deflection extent is. The magnetic field energy density gradient of Cases 9–10 is clearly much larger than that of Case 1 (compare Figure 12 with Figure 5a). Similarly, *Gui et al.* [2011] provided that there was a positive correlation between the deflection rate and the strength of the magnetic energy density gradient. Figure 13 shows the evolution of the CME on the solar-terrestrial meridian plane at four different instants (t = 1.0, 2.0, 5.0, and 10.0 h) for Case 9. From the figure, we can see that the flux rope deflects toward the HCS and finally gets into the streamer, and then propagates almost along it.

[28] Finally, we study the deflection of all of the above cases except Case B, which is only one example that deflects toward the polar region. We show the correlation between the LD extent and average transit velocity for the 11 cases in Figure 14a. Here Case C is labeled as Case 11. The average transit velocity is calculated by simply employing the ratio of the distance between the simulated 2-D CME center (say at R_2) at 10 h and its beginning (say at R_1) to 10 h, that is $(R_2-R_1)/(10\times3600)$. Wherein, the green plus marks the data of Case 11. The correlation coefficient is only –0.355795 for Cases 1–11. From the figure, we find that Cases 9–11 are far away from the majority of points. Without Cases 9–11, we find that there is a clear anticorrelation between the deflection extent and the CME average transit speed for Cases 1–8, which are based on the same background magnetic field and originated from the same source region. And the correlation coefficient increases to –0.987874 without Cases 9–11. We recall that *Gui et al.* [2011] found a weak anticorrelation between the deflection rate and the speed. Figure 14b shows the relation between the LD extent and the energy ratio E_{cme}/E_{sw} within the perturbed source region, where E is the total energy. In Table 1, we show the corresponding energy of the 11 cases. Thus, this sample shows an anticorrelation between the deflection extent and the energy ratio. The correlation coefficient is about –0.914621.

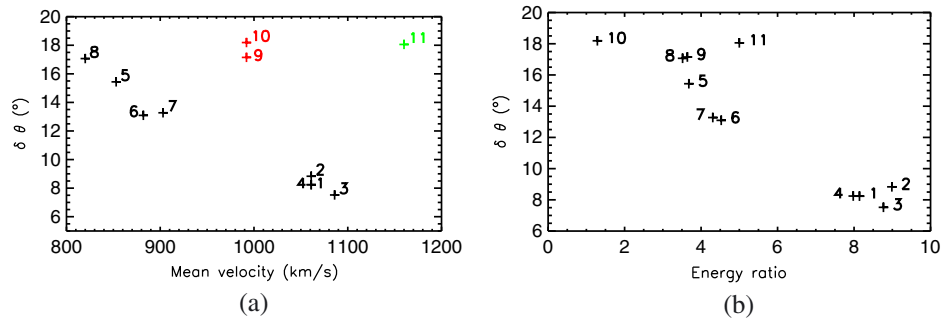

Figure 14. The plots between the LD extent versus (a) average transit velocity and (b) energy ratio.

5. Conclusion

[29] In this paper, we analyze and study the LD of CME during its outward propagation using a 3-D MHD simulation. We find that the initial magnetic polarity of CME substantially affects the evolution of the CMEs. During the solar minimum, the "parallel" CME originating from high latitude shows a clear equatorward deflection at the beginning and then propagates almost parallel to HCS. Our results show that not only the background magnetic field substantially affects the LD of CME but also initial magnetic field strength of CME is a key factor.

[30] In order to study the deflection of CME in the latitudinal direction, we choose the steady state solar wind during Carrington rotation 1922 as the background solar wind. First, we compute the steady state background solar wind by 3-D SIP-CESE MHD model, and try to mimic the 12 May 1997 halo CME event in the period using a simple spherical plasmoid model. Then we study the LD of CME and the factors influencing it based on the same background field configuration. We find that the initial magnetic polarity has the substantial effect on the propagation trajectory of CMEs. The "anti-parallel" CME from high latitude shows a clear polarward deflection, and the "parallel" CME clearly deflects toward the HCS. The HCS is located along the solar equator during this period, so this "parallel" CME shows an equatorward deflection. This study shows that during solar minimum, the CME can be easily deflected toward the low latitude region, even if it is originated from high latitude, which is in agreement with the observational study for flare-induced IP shocks [*Wei and Dryer*, 1991], it could eventually result in geoeffective events. We also quantify the effect of the initial parameters of CME model on the LD of CME. The results show that the magnetic field strength of CME substantially affects the CME's LD, and the other three parameters do have small significant effect on it. Finally, we study the influence of the background magnetic field strength on the LD of CME. Our results suggest that the stronger the background magnetic field is, the larger the LD extent is. There is an antirelation between the LD extent and the CME average transit speed and the energy ratio E_{cme}/E_{sw}. Of course, there should be other factors influencing the deflection of CME, such as coronal holes and magnetic field structure, which will be analyzed in a future paper.

[31] **Acknowledgments.** The work is jointly supported by the National Basic Research Program (973 program) under grant 2012CB825601, the Knowledge Innovation Program of the Chinese Academy of Sciences (KZZD-EW-01-4), the National Natural Science Foundation of China (41231068, 41031066, 41274179, 41274192, 41074121, 41074122, and 41374176), and the Specialized Research Fund for State Key Laboratories.

[32] Philippa Browning thanks the reviewers for their assistance in evaluating this paper.

References

Antiochos, S. K., R. B. Dahlburg, and J. A. Klimchuk (1994), The magnetic field of solar prominences, *Astrophys. J.*, *420*, 41–44, doi:10.1086/187158.

Bemporad, A., F. P. Zuccarello, C. Jacobs, M. Mierla, and S. Poedts (2012), Study of multiple coronal mass ejections at solar minimum conditions, *Solar Phys.*, *281*, 223–236, doi:10.1007/s11207-012-9999-3.

Brueckner, G. E., et al. (1998), Geomagnetic storms caused by coronal mass ejections (CMEs): March 1996 through June 1997, *Geophys. Res. Lett.*, *25*, 3019–3022, doi:10.1029/98GL00704.

Byrne, J. P., S. A. Maloney, R. T. J. McAteer, J. M. Refojo, and P. T. Gallagher (2010), Propagation of an Earth-directed coronal mass ejection in three dimensions, *Nature Commun.*, *1*, 74, doi:10.1038/ncomms1077.

Chané, E., C. Jacobs, B. van der Holst, S. Poedts, and D. Kimpe (2005), On the effect of the initial magnetic polarity and of the background wind on the evolution of CME shocks, *Astron. Astrophys.*, *432*, 331–339, doi:10.1051/0004-6361:20042005.

Chané, E., B. van der Holst, C. Jacobs, S. Poedts, and D. Kimpe (2006), Inverse and normal coronal mass ejections: Evolution up to 1 AU, *Astron. Astrophys.*, *447*, 727–733, doi:10.1051/0004-6361:20053802.

Chen, P. F., and K. Shibata (2000), An emerging flux trigger mechanism for coronal mass ejections, *Astrophys. J.*, *545*, 524–531, doi:10.1086/317803.

Cremades, H., and V. Bothmer (2004), On the three-dimensional configuration of coronal mass ejections, *Astron. Astrophys.*, *422*, 307–322, doi:10.1051/0004-6361:20035776.

Cremades, H., V. Bothmer, and D. Tripathi (2006), Properties of structured coronal mass ejections in solar cycle 23, *Adv. Space Res.*, *38*, 461–465, doi:10.1016/j.asr.2005.01.095.

Feng, X., Y. Zhou, and S. T. Wu (2007), A novel numerical implementation for solar wind modeling by the modified conservation element/solution element method, *Astrophys. J.*, *655*, 1110–1126, doi:10.1086/510121.

Feng, X., L. Yang, C. Xiang, S. T. Wu, Y. Zhou, and D. Zhong (2010), Three-dimensional solar wind modeling from the Sun to Earth by a SIP-CESE MHD model with a six-component grid, *Astrophys. J.*, *723*, 300–319, doi:10.1088/0004-637X/723/1/300.

Feynman, J., and S. F. Martin (1995), The initiation of coronal mass ejections by newly emerging magnetic flux, *J. Geophys. Res.*, *100*, 3355–3367, doi:10.1029/94JA02591.

Forbes, T. G., E. R. Priest, and P. A. Isenberg (1994), On the maximum energy release in flux-rope models of eruptive flares, *Solar Phys.*, *150*, 245–266, doi:10.1007/BF00712888.

Gui, B., C. Shen, Y. Wang, P. Ye, J. Liu, S. Wang, and X. Zhao (2011), Quantitative analysis of CME deflections in the corona, *Solar Phys.*, *271*, 111–139, doi:10.1007/s11207-011-9791-9.

Jacobs, C., and S. Poedts (2011), A polytropic model for the solar wind, *Adv. Space Res.*, *48*, 1958–1966, doi:10.1016/j.asr.2011.08.015.

Jacobs, C., S. Poedts, B. Van der Holst, and E. Chané (2005), On the effect of the background wind on the evolution of interplanetary shock waves, *Astron. Astrophys.*, *430*, 1099–1107, doi:10.1051/0004-6361:20041676.

Kilpua, E. K. J., J. Pomoell, A. Vourlidas, R. Vainio, J. Luhmann, Y. Li, P. Schroeder, A. B. Galvin, and K. Simunac (2009), STEREO observations of interplanetary coronal mass ejections and prominence deflection during solar minimum period, *Ann. Geophys.*, *27*, 4491–4503, doi:10.5194/angeo-27-4491-2009.

Liu, Y., J. A. Davies, J. G. Luhmann, A. Vourlidas, S. D. Bale, and R. P. Lin (2010a), Geometric triangulation of imaging observations to track coronal mass ejections continuously out to 1 AU, *Astrophys. J.*, *710*, L82–L87, doi:10.1088/2041-8205/710/1/L82.

Liu, Y., A. F. Thernisien, J. G. Luhmann, A. Vourlidas, J. A. Davies, R. P. Lin, and S. Bale (2010b), Reconstructing CMEs with coordinated imaging and in situ observations: Global structure, kinematics, and implications for space weather forecasting, Abstract SH23B-1861 presented at 2010 Fall Meeting, AGU.

Lugaz, N., J. N. Hernandez-Charpak, I. I. Roussev, C. J. Davis, A. Vourlidas, and J. A. Davies (2010), Determining the azimuthal properties of coronal mass ejections from multi-spacecraft remote-sensing observations with STEREO SECCHI, *Astrophys. J.*, *715*, 493–499, doi:10.1088/0004-637X/715/1/493.

MacQueen, R. M., A. J. Hundhausen, and C. W. Conover (1986), The propagation of coronal mass ejection transients, *J. Geophys. Res.*, *91*, 31–38, doi:10.1029/JA091iA01p00031.

Mikic, Z., and J. A. Linker (1994), Disruption of coronal magnetic field arcades, *Astrophys. J.*, *430*, 898–912, doi:10.1086/174460.

Odstrčil, D., M. Dryer, and Z. Smith (1996), Propagation of an interplanetary shock along the heliospheric plasma sheet, *J. Geophys. Res.*, *101*, 19,973–19,986, doi:10.1029/96JA00479.

Parker, E. N. (1963), *Interplanetary Dynamical Processes*, Wiley InterScience, New York.

Plunkett, S. P., B. J. Thompson, R. A. Howard, D. J. Michels, O. C. St. Cyr, S. J. Tappin, R. Schwenn, and P. L. Lamy (1998), LASCO observations of an Earth-directed coronal mass ejection on May 12, 1997, *Geophys. Res. Lett.*, *25*, 2477–2480, doi:10.1029/98GL50307.

Shen, C., Y. Wang, B. Gui, P. Ye, and S. Wang (2011), Kinematic evolution of a slow CME in Corona viewed by STEREO-B on 8 October 2007, *Solar Phys.*, *269*, 389–400, doi:10.1007/s11207-011-9715-8.

Smith, Z., D. Odstrcil, and M. Dryer (1998), A 2.5-dimensional MHD parametric study of interplanetary shock interactions with the heliospheric current sheet/heliospheric plasma sheet, *J. Geophys. Res.*, *103*, 20,581–20,590, doi:10.1029/98JA01994.

Thompson, B. J., S. P. Plunkett, J. B. Gurman, J. S. Newmark, O. C. St. Cyr, and D. J. Michels (1998), SOHO/EIT observations of an Earth-directed coronal mass ejection on May 12, 1997, *Geophys. Res. Lett.*, *25*, 2465–2468, doi:10.1029/98GL50429.

van der Holst, B., S. Poedts, E. Chané, C. Jacobs, G. Dubey, and D. Kimpe (2005), Modelling of solar wind, CME initiation and CME propagation, *Space Sci. Rev.*, *121*, 91–104, doi:10.1007/s11214-006-6541-7.

Wang, Y., C. Shen, S. Wang, and P. Ye (2004), Deflection of coronal mass ejection in the interplanetary medium, *Solar Phys.*, *222*, 329–343, doi:10.1023/B:SOLA.0000043576.21942.aa.

Wang, Y., X. Xue, C. Shen, P. Ye, S. Wang, and J. Zhang (2006), Impact of major coronal mass ejections on geospace during 2005 September 7–13, *Astrophys. J.*, *646*, 625–633, doi:10.1086/504676.

Wang, Y., C. Chen, B. Gui, C. Shen, P. Ye, and S. Wang (2011), Statistical study of coronal mass ejection source locations: Understanding CMEs viewed in coronagraphs, *J. Geophys. Res.*, *116*, A04104, doi:10.1029/2010JA016101.

Wei, F., and M. Dryer (1991), Propagation of solar flare-associated interplanetary shock waves in the heliospheric meridional plane, *Solar Phys.*, *132*, 373–394.

Wu, S. T., W. P. Guo, D. J. Michels, and L. F. Burlaga (1999), MHD description of the dynamical relationships between a flux rope, streamer, coronal mass ejection, and magnetic cloud: An analysis of the January 1997 Sun-Earth connection event, *J. Geophys. Res.*, *104*, 14,789–14,802, doi:10.1029/1999JA900099.

Zhang, J., J. Wang, Y. Deng, and D. Wu (2001), Magnetic flux cancellation associated with the major Solar event on 2000 July 14, *Astrophys. J.*, *548*, L99–L102, doi:10.1086/318934.

Zhou, Y. F., X. S. Feng, S. T. Wu, D. Du, F. Shen, and C. Q. Xiang (2012), Using a 3-D spherical plasmoid to interpret the Sun-to-Earth propagation of the 4 November 1997 coronal mass ejection event, *J. Geophys. Res.*, *117*, A01102, doi:10.1029/2010JA016380.

Zuccarello, F. P., A. Bemporad, C. Jacobs, M. Mierla, S. Poedts, and F. Zuccarello (2012), The role of streamers in the deflection of coronal mass ejections: Comparison between STEREO three-dimensional reconstructions and numerical simulations, *Astrophys. J.*, *744*, 66, doi:10.1088/0004-637X/744/1/66.